

**First Results from the Taiwan Axion Search Experiment with
Haloscope in the 19.47–19.84 μeV Mass Range***

Ann Author[†] and Second Author[‡]

Authors' institution and/or address

*This line break forced with *

(TASEH Collaboration)

(Dated: March 7, 2022)

Abstract

This paper presents the first results from the Taiwan Axion Search Experiment with Haloscope, a search for axions using a microwave cavity at frequencies between 4.707506 and 4.798145 GHz. Apart from the external signals, no candidates with a significance more than 3.355 were found. The experiment excludes models with the axion-two-photon coupling $|g_{a\gamma\gamma}| \gtrsim 7.7 \times 10^{-14} \text{ GeV}^{-1}$, a factor of ten above the benchmark KSVZ model for the mass range $19.47 < m_a < 19.84 \mu\text{eV}$, reaching a sensitivity three orders of magnitude better than any existing limits. It is also the first time that a haloscope-type experiment places constraints on the $|g_{a\gamma\gamma}|$ in this mass region.

CONTENTS

I. Introduction	3
A. The expected axion signal power and signal line shape	5
B. The expected noise and the signal-to-noise ratio	6
II. Experimental Setup	8
III. Calibration	9
IV. Analysis Procedure	11
A. Fast Fourier transform	12
B. Remove the structure of the background	12
C. Combine the spectra with the weighting algorithm	14
D. Merge bins	16
E. Rescan and set limits on $ g_{a\gamma\gamma} $	18
V. Analysis of the Synthetic Axion Data	19
VI. Systematic Uncertainties	20
VII. Results	23

* A footnote to the article title

† Also at Physics Department, XYZ University.

‡ Second.Author@institution.edu

31	VIII. Conclusion	25
32	Acknowledgments	26
33	A. Derivation of the Function that Models the Noise Spectrum	26
34	References	28

35 I. INTRODUCTION

36 The axion is a hypothetical particle predicted as a consequence of a solution to the strong
37 CP problem [1–3], i.e. why the CP symmetry is conserved in the strong interactions when
38 there is an explicit CP-violating term in the QCD Lagrangian. In other words, why is
39 the electric dipole moment of the neutron so tiny: $|d_n| < 1.8 \times 10^{-26} e \cdot \text{cm}$ [4, 5]? The
40 solution proposed by Peccei and Quinn is to introduce a new global Peccei-Quinn $U(1)_{\text{PQ}}$
41 symmetry that is spontaneously broken; the axion is the pseudo Nambu-Goldstone boson of
42 $U(1)_{\text{PQ}}$ [1]. Axions are abundantly produced during the QCD phase transition in the early
43 universe and may constitute the dark matter (DM). In the post-inflationary PQ symmetry
44 breaking scenario, where the PQ symmetry is broken after inflation, current calculations
45 suggest a mass range of 1–100 μeV for axions so that the cosmic axion density does not
46 exceed the observed cold DM density [6–18]. Therefore, axions are compelling because they
47 may explain at the same time puzzles that are on scales different by more than thirty orders
48 of magnitude.

49 Axions could be detected and studied via their two-photon interaction, the so-called
50 “inverse Primakoff effect”. For QCD axions, i.e. the axions proposed to solve the strong CP
51 problem, the axion-two-photon coupling constant $g_{a\gamma\gamma}$ is related to the mass of the axion
52 m_a :

$$53 \quad g_{a\gamma\gamma} = \left(\frac{g_\gamma \alpha}{\pi \Lambda^2} \right) m_a, \quad (1)$$

54 where g_γ is a dimensionless model-dependent parameter, α is the fine-structure constant,
55 $\Lambda = 78 \text{ MeV}$ is a scale parameter that can be derived from the mass and the decay constant
56 of the pion, and the ratio of the up to down quark masses. The numerical values of g_γ
57 are -0.97 and 0.36 in the Kim-Shifman-Vainshtein-Zakharov (KSVZ) [19, 20] and the Dine-
58 Fischler-Srednicki-Zhitnitsky (DFSZ) [21, 22] benchmark models, respectively.

The detectors with the best sensitivities to axions with a mass of $\approx \mu\text{eV}$, as first put forward by Sikivie [23, 24], are haloscopes consisting of a microwave cavity immersed in a strong static magnetic field and operated at a cryogenic temperature. In the presence of an external magnetic field, the ambient oscillating axion field drives the cavity and they resonate when the frequencies of the electromagnetic modes in the cavity match the microwave frequency f , where f is set by the total energy of the axion: $hf = E_a = m_a c^2 + \frac{1}{2}m_a v^2$; the signal power is further delivered to the readout probe followed by a low-noise linear amplifier. The axion mass is unknown, therefore, the cavity resonator must allow the possibility to be tuned through a range of possible axion masses. The Axion Dark Matter eXperiment (ADMX), one of the flagship dark matter search experiments, had developed and improved the cavity design and readout electronics over the years. The results from the previous versions of ADMX and the Generation 2 ADMX (ADMX G2) excluded the KSVZ benchmark model within the mass range of 1.9–4.2 μeV and the DFSZ benchmark model for the mass ranges of 2.66–3.31 and 3.9–4.1 μeV , respectively [25–31]. One of the major goals of ADMX G2 is to search for higher-mass axions in the range of 4–40 μeV (1–10 GHz), similarly for the axion experiments that were established during the last ten years. The Haloscope at Yale Sensitive to Axion Cold dark matter (HAYSTAC) had performed searches first for the mass range of 23.15–24 μeV and later at around 17 μeV ; they excluded axions with $|g_\gamma| \geq 1.38 |g_\gamma|^{\text{KSVZ}}$ for $m_a = 16.96 - 17.12$ and 17.14–17.28 μeV , respectively [32]. The Center for Axion and Precision Physics Research (CAPP) constructed and ran simultaneously several experiments targeting at different frequencies; they have pushed the limits towards the KSVZ value within a narrow mass region of 10.7126–10.7186 μeV [33]. The QUest for AXions- $a\gamma$ (QUAX- $a\gamma$) also pushed their limits close to the upper bound of the QCD axion-two-photon couplings for $m_a \approx 43 \mu\text{eV}$ [34].

This paper presents the first results and the analysis details of a search for axions for the mass range of 19.47–19.84 μeV , from the Taiwan Axion Search Experiment with Haloscope (TASEH). The expected axion signal power and signal line shape, the noise power, and the signal-to-noise ratio are described in Secs. I A–I B. An overview of the TASEH experimental setup is presented in Sec. II. Section III gives a brief description of the calibration for the whole amplification chain while Sec. IV details the analysis procedure. Section V presents the analysis of the synthetic axion data and Sec. VI discusses the systematic uncertainties that may affect the limits on the $|g_{a\gamma\gamma}|$. The final results and the conclusion are presented

91 in Sec. VII and Sec. VIII, respectively.

92 A. The expected axion signal power and signal line shape

93 The signal power extracted from a microwave cavity on resonance is given by:

$$94 \quad P_s = \left(g_\gamma^2 \frac{\alpha^2 \hbar^3 c^3 \rho_a}{\pi^2 \Lambda^4} \right) \times \left(\omega_c \frac{1}{\mu_0} B_0^2 V C_{mnl} Q_L \frac{\beta}{1 + \beta} \right), \quad (2)$$

95 where $\rho_a = 0.45 \text{ GeV/cm}^3$ is the local dark-matter density. The second set of parentheses
 96 contains parameters related to the experimental setup: the angular resonant frequency of the
 97 cavity ω_c , the vacuum permeability μ_0 , the nominal strength of the external magnetic field
 98 B_0 , the volume of the cavity V , and the loaded quality factor of the cavity $Q_L = Q_0/(1 + \beta)$,
 99 where Q_0 is the unloaded, intrinsic quality factor of the cavity and β is the coupling coefficient
 100 which determines the amount of coupling of the signal to the receiver. The form factor C_{mnl}
 101 is the normalized overlap of the electric field \vec{E} , for a particular cavity resonant mode, with
 102 the external magnetic field \vec{B} :

$$103 \quad C_{mnl} = \frac{\left[\int (\vec{B} \cdot \vec{E}_{mnl}) d^3 \mathbf{x} \right]^2}{B_0^2 V \int E_{mnl}^2 d^3 \mathbf{x}}. \quad (3)$$

104 Here, the magnetic field \vec{B} points mostly along the axial direction (z -axis) of the cavity.
 105 The field strength has a small variation along the radial and axial directions and B_0 is the
 106 nominal magnetic field strength. For cylindrical cavities, the largest form factor is from
 107 the TM_{010} mode. The expected signal power derived from the experimental parameters of
 108 TASEH (see Table I) is $P_s \simeq 1.5 \times 10^{-24} \text{ W}$ for a KSVZ axion with a mass of $19.5 \mu\text{eV}$.

109 In the direct dark matter search experiments, several assumptions are made in order to
 110 derive a signal line shape. The density and the velocity distributions of DM are related
 111 to each other through the gravitational potential. The DM in the galactic halo is assumed
 112 to be virialized. The DM halo density distribution is assumed to be spherically symmetric
 113 and close to be isothermal, which results in a velocity distribution similar to the Maxwell-
 114 Boltzmann distribution. The distribution of the measured signal frequency can be further
 115 derived from the velocity distribution after a change of variables and set $hf_a = m_a c^2$.
 116 Previous experimental results typically adopt the following function for frequency $f \geq f_a$:

$$117 \quad \mathcal{F}(f) = \frac{2}{\sqrt{\pi}} \sqrt{f - f_a} \left(\frac{3}{\alpha} \right)^{3/2} e^{\frac{-3(f-f_a)}{\alpha}}, \quad (4)$$

where $\alpha \equiv f_a \langle v^2 \rangle / c^2$. For a Maxwell-Boltzmann velocity distribution, the variance $\langle v^2 \rangle$ and the most probable velocity (speed) v_p are related to each other: $\langle v^2 \rangle = 3v_p^2/2 = (270 \text{ km/s})^2$, where $v_p = 220 \text{ km/s}$ is the local circular velocity of DM in the galactic rest frame. Equation (4) is modified if one considers that the relative velocity of the DM halo with respect to the Earth is not the same as the DM velocity in the galactic rest frame [35]. The velocity distributions shall also be truncated so that the DM velocity is not larger than the escape velocity of the Milky Way [36]. Several N-body simulations [37, 38] follow structure formation from the initial DM density perturbations to the largest halo today and take into account the merger history of the Milky Way, rather than assuming that the Milky Way is in a steady state; the simulated results suggest velocity distributions with more high-speed particles relative to the Maxwellian case [39, 40]. However, these numerical simulations contain only DM particles; an inclusion of baryons may enhance the halo's central density due to a condensation of gas towards the center of the halo via an adiabatic contraction [41, 42], or may reduce the density due to the supernova outflows, etc [43, 44].

In order to compare the results of TASEH with those of the former experiments, the analysis presented in this paper assumes an axion signal line shape by including Eq. (4) in the weights when merging the measured power from multiple frequency bins (see Sec. IV D). A signal line width $\Delta f_a = m_a \langle v^2 \rangle / h \simeq 5 \text{ kHz}$, which is much smaller than the TASEH cavity line width $f_a/Q_L \simeq 250 \text{ kHz}$, is assumed and five frequency bins are merged to perform the final analysis. For a signal line shape as described in Eq. (4), a 5-kHz bandwidth includes about 95% of the distribution. Still given the caveats above and a lack of strong evidence for any particular choice of the velocity distribution, two different scenarios are considered and their results are presented for comparison: (i) without an assumption of signal line shape, and (ii) assuming a Gaussian signal line shape with a narrower full width at half maximum (FWHM), see Sec. VII for more details.

B. The expected noise and the signal-to-noise ratio

Several physics processes can contribute to the total noise and all of them can be seen as Johnson thermal noise at some effective temperature, or the so-called system noise temperature T_{sys} . The total noise power in a bandwidth b is then:

$$P_n = k_B T_{\text{sys}} b, \quad (5)$$

where k_B is the Boltzmann constant. The system noise temperature T_{sys} has three major components:

$$T_{\text{sys}} = T_{\text{b}} + T_{\text{qn}} + T_{\text{a}}, \quad (6)$$

where

$$T_{\text{qn}} = \frac{1}{2} hf/k_B. \quad (7)$$

The three terms in Eq. (6) correspond to the effective temperatures of the following noise sources: (i) T_{b} , the blackbody radiation from the cavity at a physical temperature T_{c} , (ii) T_{qn} , the quantum noise associated with the zero-point fluctuation of the vacuum, and (iii) T_{a} , the noise added by the receiver (mainly from the first-stage amplifier). Equation (6) implies that the noise spectrum has little dependence on the frequency (white spectrum) for the narrow bandwidth considered in the experiment. However, apart from the flat baseline as described by Eq. (6), the noise spectrum observed by TASEH has an additional component with a Lorentzian shape due to the higher temperature at the cavity with respect to the temperature in the dilution refrigerator. More details may be found in Sec. II and Appendix A. The Lorentzian component will be removed from the measured spectrum and only the baseline T_{sys} will be used in the final analysis (Sec. IV).

Using the operation parameters of TASEH in Table I and the results from the calibration of readout electronics, the values of T_{b} , T_{qn} , and T_{a} are estimated to be about 0.07 K, 0.12 K, and 1.9 – 2.2 K, respectively. Therefore, the baseline value of T_{sys} for TASEH is about 2.1–2.4 K, which gives a noise power of approximately $(1.5 - 1.7) \times 10^{-19}$ W within the 5-kHz axion signal line-width, five orders of magnitude larger than the signal. Nevertheless, what matters in the analysis is the signal significance, or the so-called signal-to-noise ratio (SNR) using the standard terminology of axion experiments, i.e. the ratio of the signal power to the fluctuation in the averaged noise power spectrum σ_n .

According to Dicke’s Radiometer Equation [45], the σ_n is given by:

$$\begin{aligned} \sigma_n &= \frac{P_n}{\sqrt{N_{\text{avg}}}}, \\ &= \frac{P_n}{\sqrt{t\Delta f}}, \\ &= k_B T_{\text{sys}} \sqrt{\frac{\Delta f}{t}} \end{aligned} \quad (8)$$

where N_{avg} is the number of noise power spectra used in the average; it is related to the amount of data integration time t and the bandwidth over which a single measurement is

made Δf . The SNR will therefore be:

$$\begin{aligned} \text{SNR} &= \frac{P_s}{\sigma_n}, \\ &= \frac{P_s}{k_B T_{\text{sys}}} \sqrt{\frac{t}{\Delta f}}, \end{aligned} \quad (9)$$

Combining Eq. (2) and Eq. (9), one could see that the SNR is maximized by an experimental setup with a strong magnetic field, a large cavity volume, an efficient cavity resonant mode, a receiver with low system noise temperature, and a long integration time.

II. EXPERIMENTAL SETUP

The detector of TASEH is located at the Department of Physics, National Central University, Taiwan and housed within a cryogen-free dilution refrigerator (DR) from BlueFors. An 8-Tesla superconducting solenoid with a bore diameter of 76 mm and a length of 240 mm is integrated with the DR.

The data for the analysis presented in this paper were collected by TASEH from October 13, 2021 to November 15, 2021, and termed as the CD102 data, where CD stands for “cool down”. During the data taking, the cavity sat in the center of the magnet bore and was connected via holders to the mixing flange of the DR at a temperature of $T_{\text{mx}} \approx 27$ mK. The temperature of the cavity stayed at $T_c \simeq 155$ mK, higher with respect to the DR; it is believed that the cavity had an accidental thermal contact with the radiation shield in the DR. The cavity, made of oxygen-free high-conductivity (OFHC) copper, has an effective volume of 0.234 L and is a two-cell cylinder split along the axial direction (z -axis). The cylindrical cavity has an inner radius of 2.5 cm and a height of 12 cm. In order to maintain a smooth surface, the cavity underwent the processes of annealing, polishing, and chemical cleaning. The resonant frequency of the TM_{010} mode can be tuned over the range of 4.667–4.959 GHz via the rotation of an off-axis OFHC copper tuning rod, from the position closer to the cavity wall to the position closer to the cavity center (i.e. when the vector from the rotation axis to the tuning rod is at an angle of 0° to 180° , with respect to the vector from the cavity center to the rotation axis). The CD102 data cover the frequency range of 4.707506–4.798145 GHz. There were 839 resonant-frequency steps in total, with a frequency difference of $\Delta f_s = 95 - 115$ kHz between the steps. The value of Δf_s was kept within 10% of 105 kHz rather than a fixed value, such that the rotation angle of the tuning rod

did not need to be fine-tuned and the operation time could be minimized; a 10% variation
 of the Δf_s is found to have no impact on the $|g_{a\gamma\gamma}|$ limits. Each resonant-frequency step is
 denoted as a “scan” and the data integration time was about 32-42 minutes. The integration
 time was determined based on the target $|g_{a\gamma\gamma}|$ limits and the experimental parameters in
 Table I; the variation of the integration time aimed to remove the frequency-dependence in
 the $|g_{a\gamma\gamma}|$ limits caused by frequency dependence of the added noise T_a . The form factor C_{010}
 as defined in Eq. (3) varies from 0.64 to 0.69 over the full frequency range. The intrinsic,
 unloaded quality factor Q_0 at the cryogenic temperature ($T_c \simeq 155$ mK) is $\simeq 60000$ at the
 frequency of 4.74 GHz.

An output probe, made of a 50- Ω semi-rigid coaxial cable that was soldered to an SMA
 (SubMiniature version A) connector, was inserted into the cavity and its depth was set for
 $\beta \simeq 2$. The signal from the output probe was directed to an impedance-matched ampli-
 fication chain. The first-stage amplifier was a low noise high-electron-mobility transistor
 (HEMT) amplifier with an effective noise temperature of ≈ 2 K, mounted on the 4K flange.
 The signal was further amplified at room temperature via a three-stage post-amplifier, and
 down-converted and demodulated to in-phase (I) and quadrature (Q) components and dig-
 itized by an analog-to-digital converter with a sampling rate of 2 MHz.

A more detailed description of the TASEH detector, the operation of the data run, and
 the calibration of the gain and added noise temperature of the whole amplification chain
 can be found in Ref. [46]. See Table I for the benchmark experimental parameters that can
 be used to estimate the sensitivity of TASEH.

III. CALIBRATION

The noise is one of the most important parameters for the axion searches. Therefore,
 calibration for the amplification chain is a crucial part in the operation of TASEH. In
 order to perform a calibration, the HEMT was connected to a heat source (a 50- Ω resistor)
 instead of the cavity; various values of input currents were sent to the source to change
 its temperature monitored by a thermometer. The power from the source was delivered
 following the same transmission line as that in the axion data running. The output power
 is fitted to a first-order polynomial, as a function of the source temperature, to extract the
 gain and added noise for the amplification chain. More details of the procedure can be found

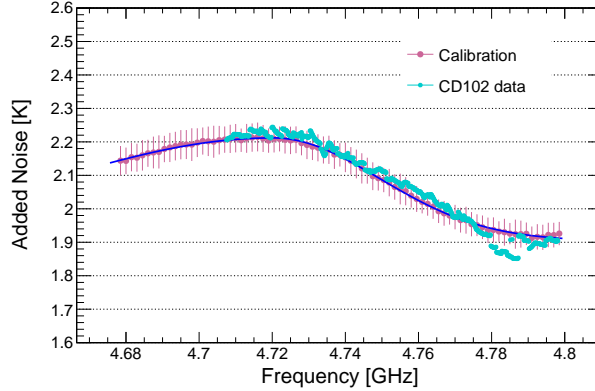
TABLE I. The benchmark experimental parameters for estimating the sensitivity of TASEH. The definitions of the parameters can be found in Sec. I. More details regarding the determination and the measurements of some of the parameters may be found in Ref. [46].

f_{lo}	4.707506 GHz
f_{hi}	4.798145 GHz
N_{step}	837
Δf_{s}	95 – 115 kHz
B_0	8 Tesla
V	0.234 L
C_{010}	0.64 – 0.69
Q_0	59000 – 65000
β	1.9 – 2.3
T_{mx}	27–28 mK
T_{c}	155 mK
T_{a}	1.9 – 2.2 K
Δf_a	5 kHz

in Ref. [46].

The calibration was carried out before, during, and after the data taking, which showed that the performance of the system was stable over time. The average of the added noise T_{a} over 19 measurements has the lowest value of 1.9 K at the frequency of 4.8 GHz and the highest value of 2.2 K at 4.72 GHz, as presented in Fig. 1. The error bars are the RMS of T_{a} and the largest RMS is used to calculate the systematic uncertainty for the limits on $|g_{a\gamma\gamma}|$. The light blue points in Fig. 1 are the noise from the axion data estimated by removing the gain and subtracting the contribution from the cavity noise, assuming that the presence of a narrow signal in the data would have no effect on the estimation. A good agreement between the results from the calibration and the ones estimated from the axion data is shown. The biggest difference is 0.076 K in the frequency range during which the data were recorded after an earthquake. The source of the difference is not understood, therefore, the difference

249 is quoted as a systematic uncertainty together with the RMS of the noise.



250

251 FIG. 1. The average added noise obtained from the calibration (pink points) and the noise esti-
 252 mated from the axion data (light blue points) as a function of frequency. The error bars on the
 253 pink points are the RMS of the T_a , as computed from the 19 measurements for each frequency in
 254 the calibration. The blue curve is obtained after performing a fit to the pink points and is used to
 255 estimate the T_a at each resonant frequency of the cavity.

256 IV. ANALYSIS PROCEDURE

257 The goal of TASEH is to find the axion signal hidden in the noise. In order to achieve
 258 this, the analysis procedure includes the following steps:

- 259 1. Perform fast Fourier transform (FFT) on the IQ time series data to obtain the
 260 frequency-domain power spectrum.
- 261 2. Apply the Savitzky-Golay (SG) filter to remove the structure of the background in the
 262 frequency-domain power spectrum.
- 263 3. Combine all the spectra from different frequency scans with the weighting algorithm.
- 264 4. Merge bins in the combined spectrum to maximize the SNR.
- 265 5. Rescan the frequency regions with candidates and set limits on the axion-two-photon
 266 coupling $|g_{a\gamma\gamma}|$ if no candidates were found.

The analysis follows the procedure similar to that developed by the HAYSTAC experiment [47]. The important points and formulas for each step are highlighted below as a reminder for the convenience of readers. Note there are a few small differences between the HAYSTAC analysis and the one presented here. In this paper, the uncertainties are considered to be uncorrelated between different frequency bins while Ref. [47] takes into account the correlation. The frequency-domain spectra processed by each intermediate step are shown. The central results of the $|g_{a\gamma\gamma}|$ limits assume the signal line shape described by Eq. (4) as in Ref. [47]. In addition, the limits without an assumption of signal line shape and the limits assuming a Gaussian signal with a narrower FWHM are shown for comparison in Sec. VII.

A. Fast Fourier transform

The in-phase $I(t)$ and quadrature $Q(t)$ components of the time-domain data were sampled and saved in the TDMS (Technical Data Management Streaming) files - a binary format developed by National Instruments. The FFT is performed to convert the data into frequency-domain power spectrum in which the measured power is calculated using the following equation:

$$\text{Power} = \frac{|\text{FFT}(I + i \cdot Q)|^2}{N \cdot 2R}, \quad (10)$$

where N is the number of data points ($N = 2000$ in the TASEH CD102 data), and R is the input resistance of the signal analyzer (50Ω). The FFT is done for every one-millisecond subspectrum data. The integration time for each frequency scan was about 32-42 minutes, which resulted in 1920000 to 2520000 subspectra; an average over these subspectra gives the averaged frequency-domain power spectrum for each scan. The frequency span in the spectrum from each resonant-frequency scan is 1.6 MHz while the resolution is 1 kHz, giving 1600 frequency bins in each spectrum.

B. Remove the structure of the background

In the absence of the axion signal, the output data spectrum is simply the noise from the cavity and the amplification chain. If axions are present in the cavity, the signal will

294 be buried in the noise because the signal power is very weak. Therefore, the structure of
 295 the raw averaged output power spectrum, as shown in the upper left panel of Fig. 2, is
 296 dominated by the noise of the system and an explanation for the structure can be found
 297 in Appendix A. The SG filter [48], a digital filter that can smooth data without distorting
 298 the signal tendency, is applied to remove the structure of the background. The SG filter
 299 is performed on the averaged spectrum of each frequency scan by fitting adjacent points
 300 of successive sub-sets of data with an n^{th} -order polynomial. The result depends on two
 301 parameters: the number of data points used for fitting, the so-called window width, and the
 302 order of the polynomial. If the window is too wide, the filter will not remove small structures,
 303 and if it is too narrow, it may kill the signal. The window and the order were first chosen
 304 during the data taking, by requiring the ratio of the raw data to the filter output consistent
 305 with unity. After the data taking, they were optimized by injecting an axion signal on top
 306 of the noise data and found that they were consistent with the original choice (see Sec. VI).

307 The raw averaged power spectrum is divided by the output of the SG filter, then unity is
 308 subtracted from the ratio to get the dimensionless normalized spectrum (lower left panel of
 309 Fig. 2). The value in each bin of the normalized spectrum is the deviation of the averaged
 310 measured power from the SG-filter output (can be considered as the averaged noise power)
 311 relative to the SG output. The symbol δ and term “RDP” are used to denote the relative
 312 deviation of power in the normalized spectrum and also in the spectra processed with rescal-
 313 ing, combining, and merging afterwards; the value can be zero, positive, or negative. In the
 314 absence of the axion signal, the RDPs in the normalized spectrum are samples drawn from
 315 a Gaussian distribution with a zero mean and a standard deviation of $1/\sqrt{N_{\text{spectra}}}$, where
 316 N_{spectra} is the number of subspectra used to compute the average (see Sec. IV A and the
 317 right panel of Fig. 2). If the axion signal exists, there will be a significant excess above zero.

318 During the data taking, the resonant frequency of the cavity was adjusted by the tuning
 319 bar so to scan a large range of frequencies and to reduce the uncertainty of the averaged
 320 noise power at the overlapped region. Therefore, the spectra of all the scans need to be
 321 combined to create one big spectrum. Before doing this, the normalized spectrum from each
 322 scan is rescaled and the rescaled spectrum is computed with the following formula:

$$\delta_{ij}^{\text{res}} = R_{ij} \delta_{ij}^{\text{norm}}, \quad (11)$$

and the standard deviation of each bin is:

$$\sigma_{ij}^{\text{res}} = R_{ij} \sigma_i^{\text{norm}}, \quad (12)$$

where

$$R_{ij} = \frac{k_B T_{\text{sys}} \Delta f_{\text{bin}}}{P_{ij}^{\text{KSVZ}} h_{ij}}, \quad (13)$$

and

$$h_{ij} = \frac{1}{1 + 4Q_{Li}^2 (f_{ij}/f_{ci} - 1)^2}. \quad (14)$$

The $\delta_{ij}^{\text{norm}}$ (δ_{ij}^{res}) and σ_i^{norm} (σ_{ij}^{res}) are the RDP and the standard deviation of the j^{th} frequency bin in the normalized (rescaled) spectrum from the i^{th} resonant-frequency scan. The value of σ_i^{norm} is derived from the spread of the RDPs over the 1600 frequency bins for the i^{th} scan. The factor R_{ij} is the ratio of the system noise power to the expected signal power of the KSVZ axion P_{ij}^{KSVZ} , with the Lorentzian cavity response h_{ij} taken into account. The system-noise temperature T_{sys} is calculated following Eq. (6), where the frequency dependence of the added-noise temperature T_a is obtained from the fitting function in Fig. 1. The Δf_{bin} is the bin width of spectrum (1 kHz). The factor h_{ij} describes the Lorentzian response of the cavity, which depends on the loaded quality factor Q_{Li} and the difference between the frequency f_{ij} in bin j and the resonant frequency f_{ci} . If a signal appears in a certain frequency bin j , its expected power will vary depending on the bin position due to the cavity's Lorentzian response. The rescaling will take into account this effect. The procedure of the normalization and the rescaling also ensures that a KSVZ axion signal will have a rescaled RDP δ_{ij}^{res} that is approximately equal to unity, if the signal power is distributed in only one frequency bin.

C. Combine the spectra with the weighting algorithm

The purpose of the weighting algorithm is to add the spectra from different resonant-frequency scans, particularly for the frequency bins that appear in multiple spectra. Each spectrum was collected with a different cavity resonant frequency. Therefore, if a signal appears in a certain frequency bin j , due to the difference in the resonant frequency and the Lorentzian response, the expected signal power will be different in each spectrum i . The weighting algorithm is expected to take this into account with a weight calculated for each

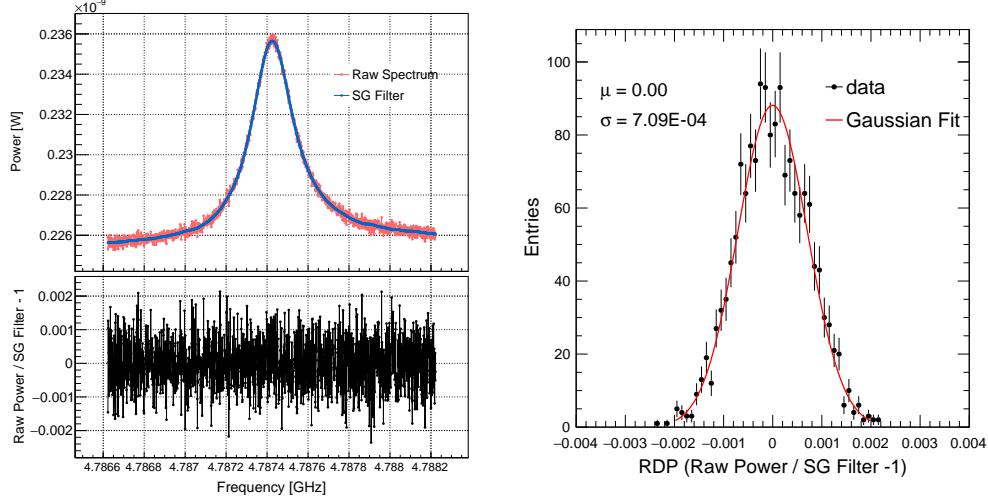


FIG. 2. Upper left panel: The raw averaged power spectrum (red points) and the output of the SG filter (blue curve) of one scan. Lower left panel: The normalized spectrum, derived by taking the ratio of the raw spectrum to the SG filter and subtracting unity from the ratio. Right plot: Histogram of the normalized spectrum (lower panel in left plot) with a Gaussian fit; there are 1600 entries in total (from the 1600 frequency bins). The fitted mean and standard deviation are shown to be consistent with the prediction when the axion signal is not present.

bin j of the rescaled spectrum i , as defined below:

$$w_{ijn} = \frac{\Gamma_{ijn}}{(\sigma_{ij}^{\text{res}})^2}. \quad (15)$$

Note, the symbol $\Gamma_{ijn} = 1$ if the j^{th} frequency bin in the i^{th} rescaled spectrum correspond to the same frequency in the n^{th} bin of the combined spectrum; otherwise, $\Gamma_{ijn} = 0$.

The RDP δ_n^{com} and the standard deviation σ_n^{com} of the n^{th} bin in the combined spectrum are calculated using Eq. (16) and Eq. (17), respectively. The $\text{SNR}_n^{\text{com}}$ is the ratio of δ_n^{com} to σ_n^{com} as given in Eq. (18). Figure 3 shows the SNR of the combined spectrum.

$$\delta_n^{\text{com}} = \frac{\sum_i \sum_j (\delta_{ij}^{\text{res}} \cdot w_{ijn})}{\sum_i \sum_j w_{ijn}}, \quad (16)$$

$$\sigma_n^{\text{com}} = \frac{\sqrt{\sum_i \sum_j (\sigma_{ij}^{\text{res}} \cdot w_{ijn})^2}}{\sum_i \sum_j w_{ijn}}, \quad (17)$$

$$\text{SNR}_n^{\text{com}} = \frac{\delta_n^{\text{com}}}{\sigma_n^{\text{com}}} = \frac{\sum_i \sum_j (\delta_{ij}^{\text{res}} \cdot w_{ijn})}{\sqrt{\sum_i \sum_j (\sigma_{ij}^{\text{res}} \cdot w_{ijn})^2}}. \quad (18)$$

For each bin n in the combined spectrum, there are m_n non-vanishing contributions to the sums above. The value of m_n ranges from 2 to 26; in general the leftmost bin or the bin with the smallest frequency (the rightmost bin or the bin with the highest frequency) in each scan has the minimum (maximum) number of m_n .

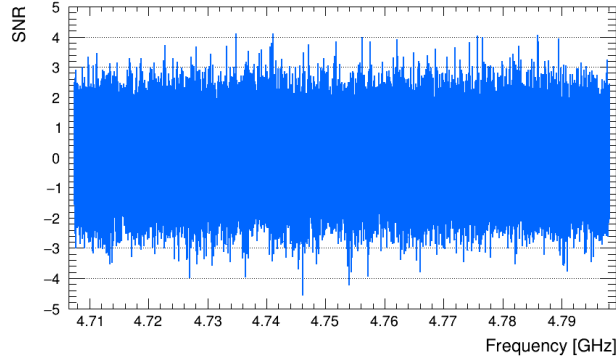


FIG. 3. The signal-to-noise ratio (SNR) calculated using Eq.(18) of the combined spectrum.

D. Merge bins

The expected axion bandwidth is about 5 kHz at the frequency of ≈ 5 GHz. In this paper, the interested frequency range is 4.707506–4.798145 GHz and the bin width is 1 kHz. Therefore, in order to maximize the SNR, a running window of five consecutive bins in the combined spectrum is applied and the five bins within each window are merged to construct a final spectrum. The purpose of using a running window is to avoid the signal power broken into different neighboring bins of the merged spectrum. The number of bins for merging is studied by injecting simulated axion signals on top of the CD102 data and optimized based on the SNR. Due to the nonuniform distribution of the axion signal [Eq. (4)], the contributing bins need to be rescaled to have the same RDP, of which the standard deviation is used to define the maximum likelihood (ML) weight for merging. The rescaling is performed by dividing the $\delta_{g+k-1}^{\text{com}}$ and $\sigma_{g+k-1}^{\text{com}}$ in the combined spectrum with an integral of the signal line shape L_k :

$$L_k = \int_{f_a + \delta f_m + (k-1)\Delta f_{\text{bin}}}^{f_a + \delta f_m + k\Delta f_{\text{bin}}} \mathcal{F}(f) df, \quad (19)$$

where the variable k is the index within the group of bins for merging, the frequency $f_a = m_a c^2/h$ is the axion frequency, and δf_m is the misalignment between f_a and the lower boundary of the g^{th} bin in the merged spectrum. The function $\mathcal{F}(f)$ has been defined in Eq. (4). In order to get a misalignment-independent line shape, instead of using an L_k that depends on δf_m , the average (\bar{L}_k) of L_k over the range of δf_m is used. In the analysis presented here, $\bar{L}_k = 0.23, 0.33, 0.21, 0.11, 0.06$ for $k = 1, \dots, 5$, respectively. The misalignment effect as mentioned in the HAYSTAC paper [47] has been studied and the results of the $|g_{a\gamma\gamma}|$ limits are found to be insensitive to this effect.

The rescaled RDP ($\delta_{g+k-1}^{\text{rs}}$) and standard deviation ($\sigma_{g+k-1}^{\text{rs}}$) are calculated:

$$\begin{aligned} \delta_{g+k-1}^{\text{rs}} &= \frac{\delta_{g+k-1}^{\text{com}}}{\bar{L}_k}, \\ \sigma_{g+k-1}^{\text{rs}} &= \frac{\sigma_{g+k-1}^{\text{com}}}{\bar{L}_k}. \end{aligned} \quad (20)$$

The variable $g = 1, \dots, N - M + 1$ is the index for the frequency bins in the final spectrum and $M = 5$ is the number of merged bin in this analysis. The numbers N and $N - M + 1$ are the total numbers of bins in the combined and final spectrum, respectively. After this rescaling procedure, a KSVZ axion signal is expected to have an RDP equal to unity for each bin of the five merged bins.

And the ML weight is defined as:

$$w_{gk} = \frac{1}{(\sigma_{g+k-1}^{\text{rs}})^2} = \frac{\bar{L}_k^2}{(\sigma_{g+k-1}^{\text{com}})^2}, \quad (21)$$

The RDP, the standard deviation, and the SNR of the merged spectrum are:

$$\delta_g^{\text{merged}} = \frac{\sum_{k=1}^M (\delta_{g+k-1}^{\text{rs}} \cdot w_{gk})}{\sum_{k=1}^M w_{gk}} = \frac{\sum_{k=1}^M \frac{\delta_{g+k-1}^{\text{com}}}{\bar{L}_k} \cdot \left(\frac{\bar{L}_k}{\sigma_{g+k-1}^{\text{com}}}\right)^2}{\sum_{k=1}^M \left(\frac{\bar{L}_k}{\sigma_{g+k-1}^{\text{com}}}\right)^2}, \quad (22)$$

$$\begin{aligned}
\sigma_g^{\text{merged}} &= \frac{\sqrt{\sum_{k=1}^M (\sigma_{g+k-1}^{\text{rs}} \cdot w_{gk})^2}}{\sum_{k=1}^M w_{gk}} = \frac{\sqrt{\sum_{k=1}^M \left(\frac{\bar{L}_k}{\sigma_{g+k-1}^{\text{com}}} \right)^2}}{\sum_{k=1}^M \left(\frac{\bar{L}_k}{\sigma_{g+k-1}^{\text{com}}} \right)^2} \\
&= \frac{1}{\sqrt{\sum_{k=1}^M \left(\frac{\bar{L}_k}{\sigma_{g+k-1}^{\text{com}}} \right)^2}}
\end{aligned} \tag{23}$$

$$\text{SNR}_g^{\text{merged}} = \frac{\delta_g^{\text{merged}}}{\sigma_g^{\text{merged}}} = \frac{\sum_{k=1}^M \frac{\delta_{g+k-1}^{\text{com}}}{L_k} \cdot \left(\frac{\bar{L}_k}{\sigma_{g+k-1}^{\text{com}}} \right)^2}{\sqrt{\sum_{k=1}^M \left(\frac{\bar{L}_k}{\sigma_{g+k-1}^{\text{com}}} \right)^2}} \tag{24}$$

E. Rescan and set limits on $|g_{a\gamma\gamma}|$

Before the collection of the CD102 data, a 5σ SNR target was chosen, which corresponds to a candidate threshold of 3.355σ at 95% confidence level (C.L.). After the merging as described in Sec. IV D, if there were any potential signal with an SNR larger than 3.355, a rescan would be proceeded to check if it were a real signal or a statistical fluctuation. The procedure of the CD102 data taking was to perform a rescan after covering every 10 MHz; the rescan was done by adjusting the tuning rod of the cavity so to match the resonant frequency to the frequency of the candidate. In total, 22 candidates with an SNR greater than 3.355 were found. Among them, 17 candidates were from the fluctuations because they were gone after a few rescans. The remaining five candidates, in the frequency ranges of 4.710170 – 4.710190 GHz and 4.747301 – 4.747380 GHz, reached an SNR greater than 4 after rescanning. The signals in the second frequency range were detected via a portable antenna outside the DR and found to come from the instruments in the laboratory, while the signals in the first frequency range were weaker but still present after turning off the external magnetic field. Therefore, these five candidates are considered external signals and no limits are placed for the above two frequency ranges. More details can be found in the TASEH instrumentation paper [46]. Figure 4 shows the SNR of the merged spectrum after including data from both the original scans and the rescans.

Since no candidates were found after the rescan, an upper limit on the signal power P_s is derived by setting P_s equal to $5\sigma_g^{\text{merged}} \times P_g^{\text{KSVZ}}$, where the σ_g^{merged} and P_g^{KSVZ} are the standard

deviation and the expected signal power for the KSVZ axion for a certain frequency bin g in the merged spectrum. Then, the 95% C.L. limits on the dimensionless parameter $|g_\gamma|$ and the axion-two-photon coupling $|g_{a\gamma\gamma}|$ could be derived according to Eq. (2) and Eq. (1). See Sec. VII for the final limits including the systematic uncertainties.

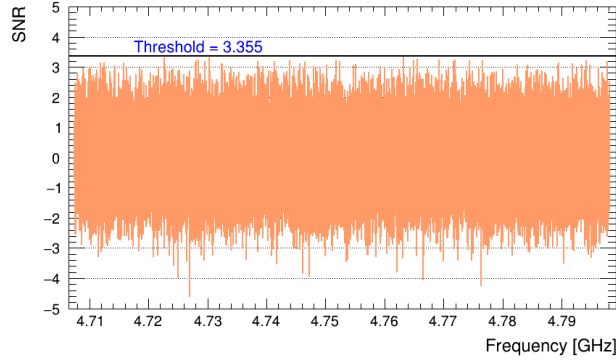


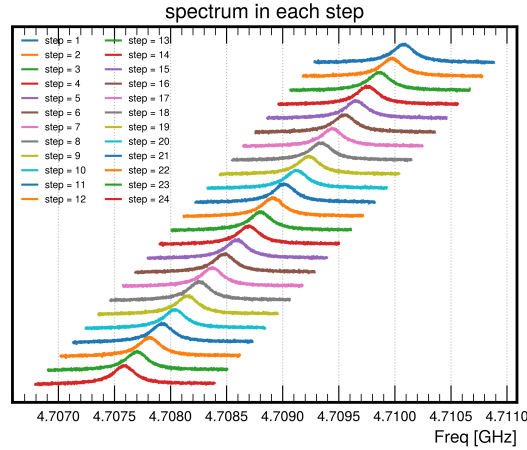
FIG. 4. The signal-to-noise ratio (SNR) calculated using Eq. (24) for the merged spectrum including data from both the original scans and the rescans. No candidate exceeds the threshold of 3.355σ (solid-black horizontal line).

V. ANALYSIS OF THE SYNTHETIC AXION DATA

After TASEH finished collecting the CD102 data on November 15, 2021, the synthetic axion signals were injected into the cavity and read out via the same transmission line and amplification chain. The procedure to generate axion-like signals is summarized in Ref. [46]. Due to the uncertainties on the losses of signal transmission lines, the synthetic axion signals are not used to perform an absolute calibration of the search sensitivity. Instead, a test with synthetic axion signals could be used to verify the procedures of data acquisition and physics analysis. The SNR of the frequency bin with maximum power from the synthetic axion signals, at 4.708970 GHz, was set to ≈ 3.35 .

The same analysis procedure as described in Sec. IV is applied to the data with synthetic axion signals. Figure 5 presents the individual raw power spectra in the 24 frequency scans. Before combining the 24 spectra, the SNR of the maximum-power bin is measured to be 3.577. After the combination of the spectra and the merging of five frequency bins, the SNRs increase to 4.74 and 6.12, respectively. In addition to the injected synthetic axion signal,

447 a candidate at 4.708006 GHz is found after merging the spectra. Since it is not possible
 448 to perform a rescan, the real axion data from the two scans that had resonant frequencies
 449 close to the candidate frequency are added so to mimic the rescan; the candidate is found
 450 to be a statistical fluctuation. Figure 6 presents the SNR after combining the spectra that
 451 share the same frequency bins and after merging five neighboring bins, respectively; the 24
 452 scans of the synthetic axion data and the two scans of the real axion data are included and
 453 processed together. The analysis results of the synthetic axion signals prove that a power
 454 excess of more than 5σ can be found at the expected frequencies via the standard analysis
 455 procedure.



456

457 FIG. 5. The raw output power spectra, before applying the SG filter, from the 24 frequency steps
 458 of the synthetic axion data. In order to show the spectra clearly, the spectra are shifted with
 459 respect to each other with an arbitrary offset in the vertical scale.

460 VI. SYSTEMATIC UNCERTAINTIES

461 The systematic uncertainties on the $|g_{a\gamma\gamma}|$ limits arise from the following sources:

- 462 • Uncertainty on the product $Q_L\beta/(1+\beta)$ in Eq. (2): In order to extract the loaded
 463 quality factor Q_L and the coupling coefficient β , a fitting of the measured results of
 464 the cavity scattering matrix was performed. A relative uncertainty of 5% is assigned
 465 to this product, after a comparison of the measurements at $T_c \simeq 155$ mK with a
 466 prediction extrapolated from the measurements at room temperature. More details

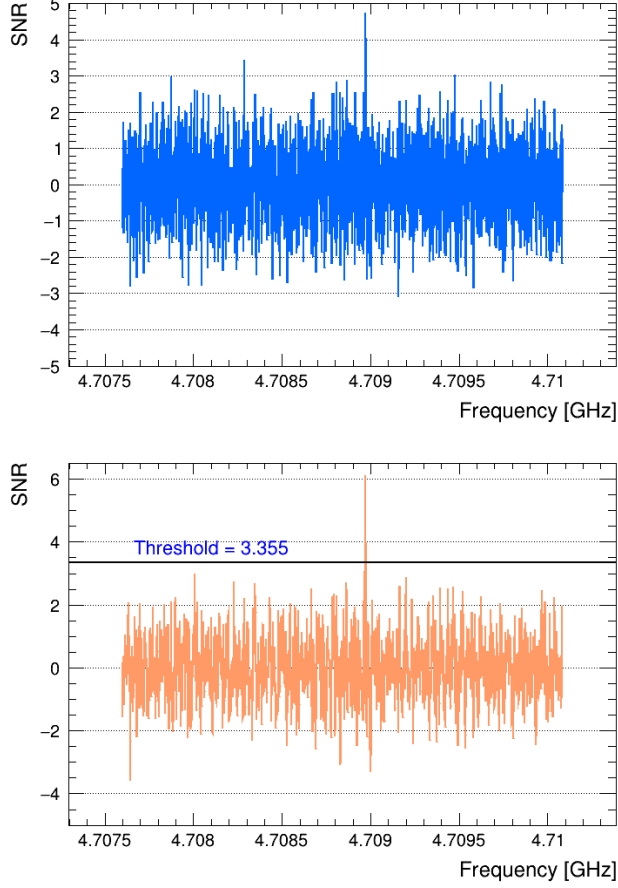


FIG. 6. The signal-to-noise ratio, from the synthetic axion data, after combining the spectra with overlapping frequencies from different scans (upper) and after merging the RDP measured in five neighboring frequency bins (lower). The procedure and the weights for combination and merging are summarized in Sec. IV C and Sec. IV D, respectively.

about the measurements of cavity properties can be found in Ref. [46].

- Uncertainty on the noise temperature T_a from the RMS of the measurements in the calibration: $\Delta T_a/T_a = 2.3\%$ (see Sec. III and Fig. 1).
- Uncertainty on the noise temperature T_a from the largest difference between the value determined by the calibration and that from the axion data: $\Delta T_a/T_a = 4\%$ (see Sec. III and Fig. 1).
- Uncertainty on the misalignment δf_m between the true axion frequency f_a and the lower bin boundaries in the merged spectrum (see Sec. IV D). MORE DESCRIPTION.

- Uncertainty from the choice of the SG-filter parameters: i.e. the window width and the order of the polynomial in the SG filter. At the beginning of the data taking, a preliminary optimization was performed: a window width of 201 bins and a 4th order polynomial were used for the first analysis of the CD102 data (see Sec. IV). This choice is kept for the central results. Nevertheless, various methods of optimization are also explored. The goal of the optimization is to find a set of SG-filter parameters that only model the noise spectrum and do not remove a real signal. The methods include:

- Minimize the difference between the two outputs returned by the SG filter, when the SG filter is applied to: (i) the real data only, and (ii) the sum of the real data and the simulated axion signals.
- Minimize the difference between the output returned by the SG filter and the function $\mathcal{G}_{\text{noise}}$ that models the noise spectrum (derived by fitting the CD102 data), when the SG filter is applied to the sum of the simulated noise based on $\mathcal{G}_{\text{noise}}$ and the simulated axion signals. See Fig. 7 for an example of the simulated spectrum, the function $\mathcal{G}_{\text{noise}}$, and the output returned by the SG filter when a 3rd-order polynomial and a window of 141 bins are chosen; the differences from all the frequency bins are summed together when performing the optimization. Figure 8 shows the difference as a function of window widths when the order of polynomial is set to three, four, and six.
- Compare the mean μ_{noise} and the width σ_{noise} of the measured power after applying the SG filter, assuming that no signal is present in the data. See Fig. 9 for an example distribution of the measured power from the averaged spectrum of a single scan; a Gaussian fit is performed to extract μ_{noise} and σ_{noise} . Given the nature of the thermal noise, the two variables are supposed to be related to each other if proper window width and order are chosen:

$$\sigma_{\text{noise}} = \frac{\mu_{\text{noise}}}{\sqrt{N_{\text{spectra}}}},$$

where N_{spectra} is the number of spectra for averaging and is related to the amount of integration time for each frequency step. In general, $N_{\text{spectra}} = 1920000 - 2520000$.

In addition, one could choose to optimize for each frequency step individually, optimize

for a certain frequency step but apply the results to all data, or optimize by adding all the frequency steps together. The deviations from the central results using different optimization approaches are in general within 1% and the maximum deviation of 1.8% on the $|g_{a\gamma\gamma}|$ limit is used as a conservative estimate of the systematic uncertainty from the SG filter.

The effects on the $|g_{a\gamma\gamma}|$ limits from these five sources are studied and added in quadrature to obtain the total systematic uncertainty. The systematic uncertainties on the $|g_{a\gamma\gamma}|$ limits are displayed together with the central results in Sec. VII. Overall the total relative systematic uncertainty is $\approx XXX\%$.

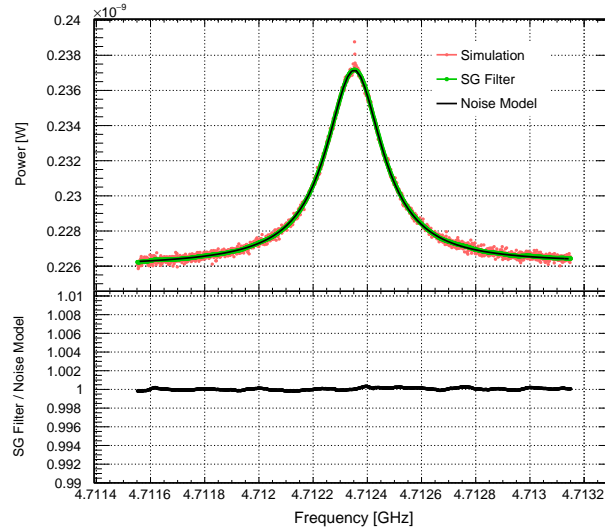


FIG. 7. Upper panel: The simulated spectrum (red), including the axion signal and the noise, is overlaid with the function that models the noise $\mathcal{G}_{\text{noise}}$ (black) and the output returned by the SG filter (green). Lower panel: The ratio of the output returned by the SG filter to the function $\mathcal{G}_{\text{noise}}$.

VII. RESULTS

Figure 10 shows the limits on the axion-two-photon coupling $|g_{a\gamma\gamma}|$ and the ratio of the limits on the dimensionless parameter $|g_\gamma|$ with respect to the KSVZ benchmark value ($|g_{\text{KSVZ}}| = 0.97$). The blue error band indicates the systematic uncertainties as discussed in Sec. VI. No limits are placed for the frequency ranges of 4.710170 – 4.710190 GHz and 4.747301 – 4.747380 GHz, which correspond to the external signals during the collection of

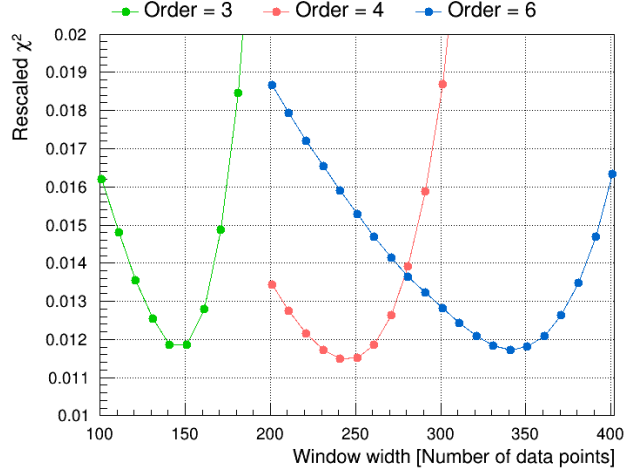


FIG. 8. The difference between the output returned by the SG filter and the function that models the noise spectrum, when various values of window widths and a 3rd, a 4th, or a 6th-order polynomial are applied in the SG filter. In this figure, the best choice is a 4th-order polynomial with a window width of 241 data points (bins).

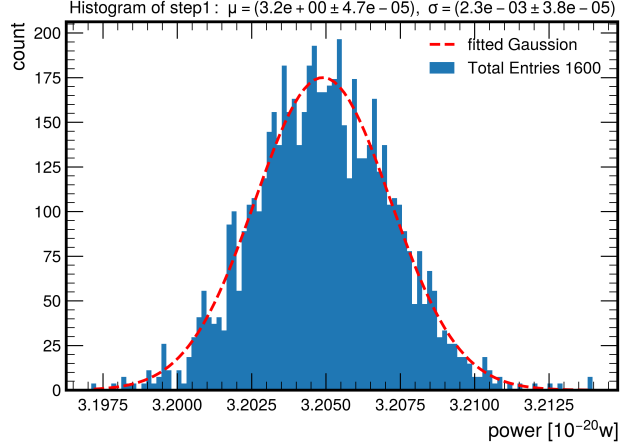


FIG. 9. An example of the distribution of the measured power after applying the SG filter, when the cavity resonant frequency is 4.798147 GHz. The distribution contains 1600 entries and each entry corresponds to the measured power in one frequency bin, averaged over 1920000 subspectra. The mean and the width returned by a Gaussian fit to the distribution are used to determine the best choice of SG parameters. The mean $\mu_{\text{noise}} = 3.2 \times 10^{-20}$ W in a 1-kHz frequency bin would imply a noise temperature of 2.3 K.

the CD102 data. The limits on $|g_{a\gamma\gamma}|$ range from $4.4 \times 10^{-14} \text{ GeV}^{-1}$ to $8.3 \times 10^{-14} \text{ GeV}^{-1}$, with an average value of $7.7 \times 10^{-14} \text{ GeV}^{-1}$; the lowest value comes from the frequency bins with additional eight times more data from the rescans, while the highest value comes from the frequency bins near the boundaries of the spectrum. Figure 11 displays the $|g_{a\gamma\gamma}|$ limits obtained by TASEH together with those from the previous searches. The results of TASEH exclude the models with the axion-two-photon coupling $|g_{a\gamma\gamma}| \gtrsim 7.7 \times 10^{-14} \text{ GeV}^{-1}$, a factor of ten above the benchmark KSVZ model for the mass range $19.47 < m_a < 19.84 \mu\text{eV}$ (corresponding to the frequency range of $4.707506 < f_a < 4.798145 \text{ GHz}$).

The central results shown in Figs. 10–11 are obtained assuming an axion signal line shape that follows Eq. (4). The analysis that merges bins without assuming a signal line shape results in $\approx 5.5\%$ larger values on the $|g_{a\gamma\gamma}|$ limits. If a Gaussian signal line shape with an FWHM of 2.5 kHz, about half of the axion line width in Eq. (4), is assumed instead, the limits will be $\approx 3.8\%$ smaller than the central results.

VIII. CONCLUSION

This paper presents the first results of a search for axions for the mass range $19.47 < m_a < 19.84 \mu\text{eV}$, using the CD102 data collected by the Taiwan Axion Search Experiment with Haloscope from October 13, 2021 to November 15, 2021. Apart from the external signals, no candidates with a significance more than 3.355 were found. The experiment excludes models with the axion-two-photon coupling $|g_{a\gamma\gamma}| \gtrsim 7.7 \times 10^{-14} \text{ GeV}^{-1}$ at 95% C.L., a factor of ten above the benchmark KSVZ model. The sensitivity on $|g_{a\gamma\gamma}|$ reached by TASEH is three orders of magnitude better than the existing limits. It is also the first time that a haloscope-type experiment places constraints in this mass region. The synthetic axion signals were injected after the collection of data and the successful results validate the data acquisition and the analysis procedure.

The target of TASEH is to search for axions for the mass range of $16.5\text{--}20.7 \mu\text{eV}$ corresponding to a frequency range of 4–5 GHz, with a capability to be extended to 2.5–6 GHz in the future. In the coming years, several upgrades are expected, including: the use of a quantum-limited Josephson parametric amplifier as the first-stage amplifier, the replacement of the existing dilution refrigerator with a new one that has a magnetic field of about 9 Tesla and a larger bore size, and the development of a new cavity with a significantly

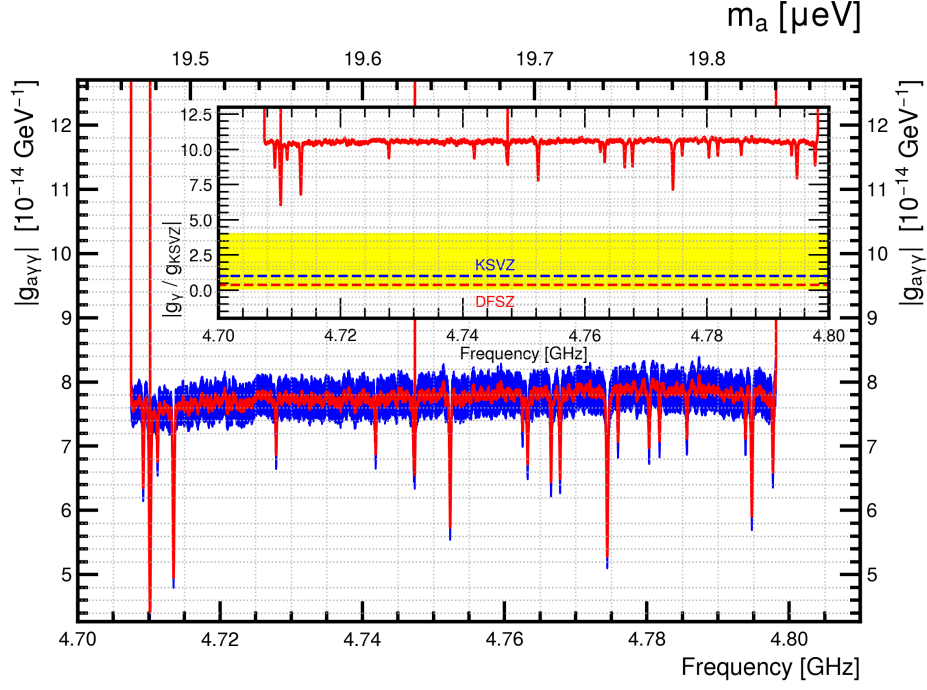


FIG. 10. The limits on $|g_{a\gamma\gamma}|$ and the ratio of the limits on $|g_\gamma|$ relative to $|g_{\text{KSVZ}}| = 0.97$ (inset) for the frequency range of 4.707506–4.798145 GHz. The blue error band indicates the systematic uncertainties as discussed in Sec. VI. The yellow band in the inset shows the allowed region of $|g_\gamma|$ vs. m_a from various QCD axion models, while the blue and red dashed lines are the values predicted by the KSVZ and DFSZ benchmark models, respectively

larger effective volume. With the improvements of the experimental setup and several years of data taking, TASEH is expected to probe the QCD axion band in the target mass range.

ACKNOWLEDGMENTS

Appendix A: Derivation of the Function that Models the Noise Spectrum

The Hamiltonian of a single-mode cavity is

$$H = \hbar\omega_c(C^\dagger C + \frac{1}{2}), \quad (\text{A1})$$

where $\omega_c/2\pi$ is the cavity resonant frequency and C is the annihilation operator of the inner cavity field. The cavity field is coupled to the modes A of a transmission line with the rate κ_2 . The cavity field is also coupled to the environment modes B with the rate κ_0 . Based on

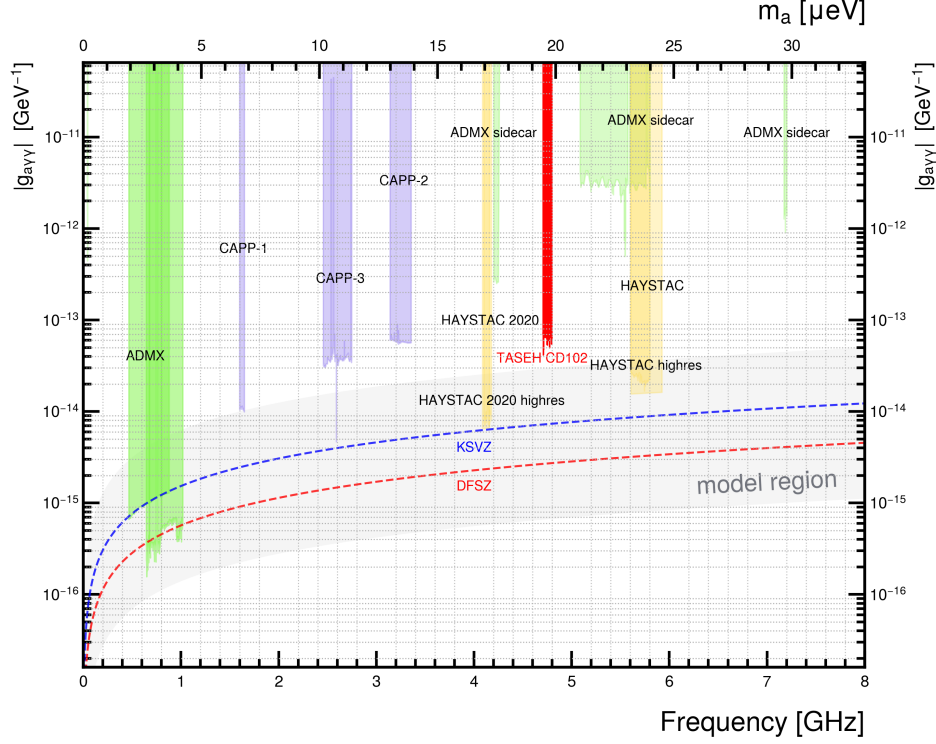


FIG. 11. The limits on the axion-two-photon coupling $|g_{a\gamma\gamma}|$ for the frequency ranges of 0–8 GHz, from the CD102 data of TASEH and previous searches performed by the ADMX, CAPP, and HAYSTAC Collaborations. The gray band indicates the allowed region of $|g_{a\gamma\gamma}|$ vs. m_a from various QCD axion models while the blue and red dashed lines are the values predicted by the KSVZ and DFSZ benchmark models, respectively.

the model of Fig. 12 and the input-output theory, the equation of motion for C is obtained:

$$\frac{dC}{dt} = -i\omega_c C - \frac{\kappa_2 + \kappa_0}{2} C + \sqrt{\kappa_2} A_{\text{in}} + \sqrt{\kappa_0} B_{\text{in}}. \quad (\text{A2})$$

A boundary condition holds for the transmission modes:

$$A_{\text{out}} = \sqrt{\kappa_2} C - A_{\text{in}}. \quad (\text{A3})$$

Considering working in a rotating frame of the signal frequency ω near ω_c , the equation of motion becomes:

$$-i\omega C + \frac{dC}{dt} = -i\omega_c C - \frac{\kappa_2 + \kappa_0}{2} C + \sqrt{\kappa_2} A_{\text{in}} + \sqrt{\kappa_0} B_{\text{in}}. \quad (\text{A4})$$

The steady state solution for the cavity field is:

$$C = \frac{\sqrt{\kappa_2} A_{\text{in}} + \sqrt{\kappa_0} B_{\text{in}}}{-i(\omega - \omega_c) + \frac{\kappa_2 + \kappa_0}{2}}. \quad (\text{A5})$$

By substituting Eq. (A5) into Eq. (A3), the reflected modes of the transmission line A_{out} are expressed in terms of the input modes of the transmission line A_{in} and the environment B_{in} :

$$\begin{aligned}
A_{\text{out}} &= \frac{i(\omega - \omega_c) + \frac{\kappa_2 - \kappa_0}{2}}{-i(\omega - \omega_c) + \frac{\kappa_2 + \kappa_0}{2}} A_{\text{in}} + \frac{\sqrt{\kappa_2 \kappa_0}}{-i(\omega - \omega_c) + \frac{\kappa_2 + \kappa_0}{2}} B_{\text{in}} \\
&= \frac{-(\omega - \omega_c)^2 + \frac{\kappa_2^2 - \kappa_0^2}{4} + i\kappa_2(\omega - \omega_c)}{(\omega - \omega_c)^2 + (\frac{\kappa_2 + \kappa_0}{2})^2} A_{\text{in}} \\
&\quad + \frac{\sqrt{\kappa_2 \kappa_0} \frac{\kappa_2 + \kappa_0}{2} + i\sqrt{\kappa_2 \kappa_0}(\omega - \omega_c)}{(\omega - \omega_c)^2 + (\frac{\kappa_2 + \kappa_0}{2})^2} B_{\text{in}}.
\end{aligned} \tag{A6}$$

Therefore, the autocorrelation of A_{out} is related to those of A_{in} and B_{in} :

$$\begin{aligned}
\langle A_{\text{out}}^\dagger A_{\text{out}} \rangle &= \frac{[(\omega - \omega_c)^2 - \frac{\kappa_2^2 - \kappa_0^2}{4}]^2 + \kappa_2^2(\omega - \omega_c)^2}{[(\omega - \omega_c)^2 + (\frac{\kappa_2 + \kappa_0}{2})^2]^2} \langle A_{\text{in}}^\dagger A_{\text{in}} \rangle \\
&\quad + \frac{\kappa_2 \kappa_0 (\frac{\kappa_2 + \kappa_0}{2})^2 + \kappa_2 \kappa_0 (\omega - \omega_c)^2}{[(\omega - \omega_c)^2 + (\frac{\kappa_2 + \kappa_0}{2})^2]^2} \langle B_{\text{in}}^\dagger B_{\text{in}} \rangle.
\end{aligned} \tag{A7}$$

The spectrum from the cavity $S(\omega)$ is found to be related to the spectrum of the readout transmission line $S_{\text{rt}}(\omega)$ and the spectrum of the cavity environment $S_{\text{cav}}(\omega)$:

$$\begin{aligned}
S(\omega) &= \frac{[(\omega - \omega_c)^2 - \frac{\kappa_2^2 - \kappa_0^2}{4}]^2 + \kappa_2^2(\omega - \omega_c)^2}{[(\omega - \omega_c)^2 + (\frac{\kappa_2 + \kappa_0}{2})^2]^2} S_{\text{rt}}(\omega) \\
&\quad + \frac{\kappa_2 \kappa_0 (\frac{\kappa_2 + \kappa_0}{2})^2 + \kappa_2 \kappa_0 (\omega - \omega_c)^2}{[(\omega - \omega_c)^2 + (\frac{\kappa_2 + \kappa_0}{2})^2]^2} S_{\text{cav}}(\omega).
\end{aligned} \tag{A8}$$

As the the readout transmission line and the cavity environment are both in thermal states, i.e. $S_{\text{rt}}(\omega) = [n_{\text{BE}}(T_{\text{rt}}) + 1/2] \hbar\omega$ and $S_{\text{cav}}(\omega) = [n_{\text{BE}}(T_{\text{cav}}) + 1/2] \hbar\omega$, where n_{BE} is the mean photon number given by the Bose-Einstein distribution, $S(\omega)$ is white if $T_{\text{cav}} = T_{\text{rt}}$, and Lorentzian if $T_{\text{cav}} \gg T_{\text{rt}}$.

-
- [1] R. D. Peccei and H. R. Quinn, CP conservation in the presence of pseudoparticles, Phys. Rev. Lett. **38**, 1440 (1977).
- [2] S. Weinberg, A new light boson?, Phys. Rev. Lett. **40**, 223 (1978).
- [3] F. Wilczek, Problem of strong p and t invariance in the presence of instantons, Phys. Rev. Lett. **40**, 279 (1978).
- [4] C. Abel *et al.* (nEDM), Measurement of the permanent electric dipole moment of the neutron, Phys. Rev. Lett. **124**, 081803 (2020), arXiv:2001.11966 [hep-ex].

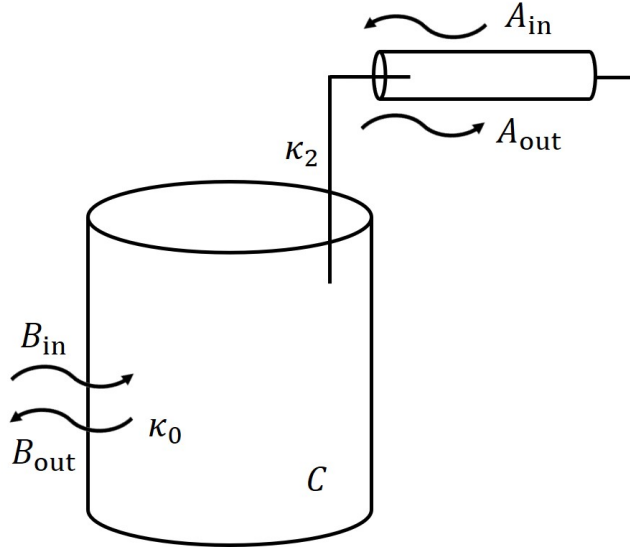


FIG. 12. A cavity is coupled to the modes of transmission line A with the rate κ_2 and the modes of environment B with the rate κ_0 .

- [5] P. D. Group, P. A. Zyla, R. M. Barnett, J. Beringer, O. Dahl, D. A. Dwyer, D. E. Groom, C. J. Lin, K. S. Lugovsky, E. Pianori, D. J. Robinson, C. G. Wohl, W. M. Yao, K. Agashe, G. Aielli, B. C. Allanach, C. Amsler, M. Antonelli, E. C. Aschenauer, D. M. Asner, H. Baer, S. Banerjee, L. Baudis, C. W. Bauer, J. J. Beatty, V. I. Belousov, S. Bethke, A. Bettini, O. Biebel, K. M. Black, E. Blucher, O. Buchmuller, V. Burkert, M. A. Bychkov, R. N. Cahn, M. Carena, A. Cecucci, A. Cerri, D. Chakraborty, R. S. Chivukula, G. Cowan, G. D'Ambrosio, T. Damour, D. de Florian, A. de Gouvêa, T. DeGrand, P. de Jong, G. Dissertori, B. A. Dobrescu, M. D'Onofrio, M. Doser, M. Drees, H. K. Dreiner, P. Eerola, U. Egede, S. Eidelman, J. Ellis, J. Erler, V. V. Ezhela, W. Fetscher, B. D. Fields, B. Foster, A. Freitas, H. Gallagher, L. Garren, H. J. Gerber, G. Gerbier, T. Gershon, Y. Gershtein, T. Gherghetta, A. A. Godizov, M. C. Gonzalez-Garcia, M. Goodman, C. Grab, A. V. Gritsan, C. Grojean, M. Grünewald, A. Gurtu, T. Gutsche, H. E. Haber, C. Hanhart, S. Hashimoto, Y. Hayato, A. Hebecker, S. Heinemeyer, B. Heltsley, J. J. Hernández-Rey, K. Hikasa, J. Hisano, A. Höcker, J. Holder, A. Holtkamp, J. Huston, T. Hyodo, K. F. Johnson, M. Kado, M. Karliner, U. F. Katz, M. Kenzie, V. A. Khoze, S. R. Klein, E. Klempt, R. V. Kowalewski, F. Krauss, M. Kreps, B. Krusche, Y. Kwon, O. Lahav, J. Laiho, L. P. Lellouch, J. Lesgourgues, A. R. Liddle, Z. Ligeti, C. Lippmann, T. M. Liss, L. Littenberg, C. Lourenço, S. B. Lugovsky, A. Lusiani, Y. Makida, F. Mal-

toni, T. Mannel, A. V. Manohar, W. J. Marciano, A. Masoni, J. Matthews, U. G. Meißner, M. Mikhasenko, D. J. Miller, D. Milstead, R. E. Mitchell, K. Mönig, P. Molaro, F. Moortgat, M. Moskvic, K. Nakamura, M. Narain, P. Nason, S. Navas, M. Neubert, P. Nevski, Y. Nir, K. A. Olive, C. Patrignani, J. A. Peacock, S. T. Petcov, V. A. Petrov, A. Pich, A. Piepke, A. Pomarol, S. Profumo, A. Quadt, K. Rabbertz, J. Rademacker, G. Raffelt, H. Ramani, M. Ramsey-Musolf, B. N. Ratcliff, P. Richardson, A. Ringwald, S. Roesler, S. Rolli, A. Romaniouk, L. J. Rosenberg, J. L. Rosner, G. Rybka, M. Ryskin, R. A. Ryutin, Y. Sakai, G. P. Salam, S. Sarkar, F. Sauli, O. Schneider, K. Scholberg, A. J. Schwartz, J. Schwiening, D. Scott, V. Sharma, S. R. Sharpe, T. Shutt, M. Silari, T. Sjöstrand, P. Skands, T. Skwarnicki, G. F. Smoot, A. Soffer, M. S. Sozzi, S. Spanier, C. Spiering, A. Stahl, S. L. Stone, Y. Sumino, T. Sumiyoshi, M. J. Syphers, F. Takahashi, M. Tanabashi, J. Tanaka, M. Taševský, K. Terashi, J. Terning, U. Thoma, R. S. Thorne, L. Tiator, M. Titov, N. P. Tkachenko, D. R. Tovey, K. Trabelsi, P. Urquijo, G. Valencia, R. Van de Water, N. Varelas, G. Venanzoni, L. Verde, M. G. Vincter, P. Vogel, W. Vogelsang, A. Vogt, V. Vorobyev, S. P. Wakely, W. Walkowiak, C. W. Walter, D. Wands, M. O. Wascko, D. H. Weinberg, E. J. Weinberg, M. White, L. R. Wiencke, S. Willocq, C. L. Woody, R. L. Workman, M. Yokoyama, R. Yoshida, G. Zanderighi, G. P. Zeller, O. V. Zenin, R. Y. Zhu, S. L. Zhu, F. Zimmermann, J. Anderson, T. Basaglia, V. S. Lugovsky, P. Schaffner, and W. Zheng, Review of Particle Physics, Progress of Theoretical and Experimental Physics **2020**, 10.1093/ptep/ptaa104 (2020), 083C01, <https://academic.oup.com/ptep/article-pdf/2020/8/083C01/34673722/ptaa104.pdf>.

[6] S. Borsanyi *et al.*, Calculation of the axion mass based on high-temperature lattice quantum chromodynamics, Nature **539**, 69 (2016), arXiv:1606.07494 [hep-lat].

[7] M. Dine, P. Draper, L. Stephenson-Haskins, and D. Xu, Axions, Instantons, and the Lattice, Phys. Rev. D **96**, 095001 (2017), arXiv:1705.00676 [hep-ph].

[8] T. Hiramatsu, M. Kawasaki, T. Sekiguchi, M. Yamaguchi, and J. Yokoyama, Improved estimation of radiated axions from cosmological axionic strings, Phys. Rev. D **83**, 123531 (2011), arXiv:1012.5502 [hep-ph].

[9] M. Kawasaki, K. Saikawa, and T. Sekiguchi, Axion dark matter from topological defects, Phys. Rev. D **91**, 065014 (2015), arXiv:1412.0789 [hep-ph].

[10] E. Berkowitz, M. I. Buchoff, and E. Rinaldi, Lattice QCD input for axion cosmology, Phys. Rev. D **92**, 034507 (2015), arXiv:1505.07455 [hep-ph].

- [11] L. Fleury and G. D. Moore, Axion dark matter: strings and their cores, JCAP **01**, 004, arXiv:1509.00026 [hep-ph].
- [12] C. Bonati, M. D’Elia, M. Mariti, G. Martinelli, M. Mesiti, F. Negro, F. Sanfilippo, and G. Villadoro, Axion phenomenology and θ -dependence from $N_f = 2 + 1$ lattice QCD, JHEP **03**, 155, arXiv:1512.06746 [hep-lat].
- [13] P. Petreczky, H.-P. Schadler, and S. Sharma, The topological susceptibility in finite temperature QCD and axion cosmology, Phys. Lett. B **762**, 498 (2016), arXiv:1606.03145 [hep-lat].
- [14] G. Ballesteros, J. Redondo, A. Ringwald, and C. Tamarit, Unifying inflation with the axion, dark matter, baryogenesis and the seesaw mechanism, Phys. Rev. Lett. **118**, 071802 (2017), arXiv:1608.05414 [hep-ph].
- [15] V. B. . Klaer and G. D. Moore, The dark-matter axion mass, JCAP **11**, 049, arXiv:1708.07521 [hep-ph].
- [16] M. Buschmann, J. W. Foster, and B. R. Safdi, Early-Universe Simulations of the Cosmological Axion, Phys. Rev. Lett. **124**, 161103 (2020), arXiv:1906.00967 [astro-ph.CO].
- [17] M. Gorghetto, E. Hardy, and G. Villadoro, More axions from strings, SciPost Phys. **10**, 050 (2021), arXiv:2007.04990 [hep-ph].
- [18] M. Buschmann, J. W. Foster, A. Hook, A. Peterson, D. E. Willcox, W. Zhang, and B. R. Safdi, Dark Matter from Axion Strings with Adaptive Mesh Refinement, (2021), arXiv:2108.05368 [hep-ph].
- [19] J. E. Kim, Weak Interaction Singlet and Strong CP Invariance, Phys. Rev. Lett. **43**, 103 (1979).
- [20] M. A. Shifman, A. I. Vainshtein, and V. I. Zakharov, Can Confinement Ensure Natural CP Invariance of Strong Interactions?, Nucl. Phys. B **166**, 493 (1980).
- [21] M. Dine, W. Fischler, and M. Srednicki, A Simple Solution to the Strong CP Problem with a Harmless Axion, Phys. Lett. B **104**, 199 (1981).
- [22] A. R. Zhitnitsky, On Possible Suppression of the Axion Hadron Interactions. (In Russian), Sov. J. Nucl. Phys. **31**, 260 (1980).
- [23] P. Sikivie, Experimental tests of the ”invisible” axion, Phys. Rev. Lett. **51**, 1415 (1983).
- [24] P. Sikivie, Detection rates for ”invisible”-axion searches, Phys. Rev. D **32**, 2988 (1985).
- [25] C. Hagmann, D. Kinion, W. Stoeffl, K. van Bibber, E. Daw, H. Peng, L. J. Rosenberg, J. LaVeigne, P. Sikivie, N. S. Sullivan, D. B. Tanner, F. Nezrick, M. S. Turner, D. M. Moltz,

- J. Powell, and N. A. Golubev, Results from a high-sensitivity search for cosmic axions, *Phys. Rev. Lett.* **80**, 2043 (1998).
- [26] S. J. Asztalos, E. Daw, H. Peng, L. J. Rosenberg, D. B. Yu, C. Hagmann, D. Kinion, W. Stoeffl, K. van Bibber, J. LaVeigne, P. Sikivie, N. S. Sullivan, D. B. Tanner, F. Nezrick, and D. M. Moltz, Experimental constraints on the axion dark matter halo density, *The Astrophysical Journal* **571**, L27 (2002).
- [27] S. J. Asztalos, R. F. Bradley, L. Duffy, C. Hagmann, D. Kinion, D. M. Moltz, L. J. Rosenberg, P. Sikivie, W. Stoeffl, N. S. Sullivan, D. B. Tanner, K. van Bibber, and D. B. Yu, Improved rf cavity search for halo axions, *Phys. Rev. D* **69**, 011101 (2004).
- [28] S. J. Asztalos, G. Carosi, C. Hagmann, D. Kinion, K. van Bibber, M. Hotz, L. J. Rosenberg, G. Rybka, J. Hoskins, J. Hwang, P. Sikivie, D. B. Tanner, R. Bradley, and J. Clarke, Squid-based microwave cavity search for dark-matter axions, *Phys. Rev. Lett.* **104**, 041301 (2010).
- [29] N. Du, N. Force, R. Khatiwada, E. Lentz, R. Ottens, L. J. Rosenberg, G. Rybka, G. Carosi, N. Woollett, D. Bowring, A. S. Chou, A. Sonnenschein, W. Wester, C. Boutan, N. S. Oblath, R. Bradley, E. J. Daw, A. V. Dixit, J. Clarke, S. R. O’Kelley, N. Crisosto, J. R. Gleason, S. Jois, P. Sikivie, I. Stern, N. S. Sullivan, D. B. Tanner, and G. C. Hilton (ADMX Collaboration), Search for invisible axion dark matter with the axion dark matter experiment, *Phys. Rev. Lett.* **120**, 151301 (2018).
- [30] T. Braine, R. Cervantes, N. Crisosto, N. Du, S. Kimes, L. J. Rosenberg, G. Rybka, J. Yang, D. Bowring, A. S. Chou, R. Khatiwada, A. Sonnenschein, W. Wester, G. Carosi, N. Woollett, L. D. Duffy, R. Bradley, C. Boutan, M. Jones, B. H. LaRoque, N. S. Oblath, M. S. Taubman, J. Clarke, A. Dove, A. Eddins, S. R. O’Kelley, S. Nawaz, I. Siddiqi, N. Stevenson, A. Agrawal, A. V. Dixit, J. R. Gleason, S. Jois, P. Sikivie, J. A. Solomon, N. S. Sullivan, D. B. Tanner, E. Lentz, E. J. Daw, J. H. Buckley, P. M. Harrington, E. A. Henriksen, and K. W. Murch (ADMX Collaboration), Extended search for the invisible axion with the axion dark matter experiment, *Phys. Rev. Lett.* **124**, 101303 (2020).
- [31] C. Bartram *et al.* (ADMX Collaboration), Search for Invisible Axion Dark Matter in the 3.3–4.2 μeV Mass Range, *Phys. Rev. Lett.* **127**, 261803 (2021).
- [32] K. M. Backes, D. A. Palken, S. A. Kenany, B. M. Brubaker, S. B. Cahn, A. Droster, G. C. Hilton, S. Ghosh, H. Jackson, S. K. Lamoreaux, and et al., A quantum enhanced search for dark matter axions, *Nature* **590**, 238–242 (2021).

- [33] O. Kwon, D. Lee, W. Chung, D. Ahn, H. Byun, F. Caspers, H. Choi, J. Choi, Y. Chong, H. Jeong, J. Jeong, J. E. Kim, J. Kim, i. m. c. b. u. Kutlu, J. Lee, M. Lee, S. Lee, A. Matlashov, S. Oh, S. Park, S. Uchaikin, S. Youn, and Y. K. Semertzidis, First results from an axion haloscope at capp around $10.7 \mu\text{eV}$, Phys. Rev. Lett. **126**, 191802 (2021).
- [34] D. Alesini, C. Braggio, G. Carugno, N. Crescini, D. D’Agostino, D. Di Gioacchino, R. Di Vora, P. Falferi, U. Gambardella, C. Gatti, G. Iannone, C. Ligi, A. Lombardi, G. Maccarrone, A. Ortolan, R. Pengo, A. Rettaroli, G. Ruoso, L. Taffarello, and S. Tocci, Search for invisible axion dark matter of mass $m_a = 43 \mu\text{eV}$ with the quax- $a\gamma$ experiment, Phys. Rev. D **103**, 102004 (2021).
- [35] M. S. Turner, Periodic signatures for the detection of cosmic axions, Phys. Rev. D **42**, 3572 (1990).
- [36] M. Lisanti, Lectures on Dark Matter Physics, in *Theoretical Advanced Study Institute in Elementary Particle Physics: New Frontiers in Fields and Strings* (2017) pp. 399–446, arXiv:1603.03797 [hep-ph].
- [37] J. Diemand, M. Kuhlen, P. Madau, M. Zemp, B. Moore, D. Potter, and J. Stadel, Clumps and streams in the local dark matter distribution, Nature **454**, 735 (2008), arXiv:0805.1244 [astro-ph].
- [38] V. Springel, J. Wang, M. Vogelsberger, A. Ludlow, A. Jenkins, A. Helmi, J. F. Navarro, C. S. Frenk, and S. D. M. White, The Aquarius Project: the subhalos of galactic halos, Mon. Not. Roy. Astron. Soc. **391**, 1685 (2008), arXiv:0809.0898 [astro-ph].
- [39] J. F. Navarro, C. S. Frenk, and S. D. M. White, The Structure of cold dark matter halos, Astrophys. J. **462**, 563 (1996), arXiv:astro-ph/9508025.
- [40] A. Burkert, The Structure of dark matter halos in dwarf galaxies, Astrophys. J. Lett. **447**, L25 (1995), arXiv:astro-ph/9504041.
- [41] G. R. Blumenthal, S. M. Faber, R. Flores, and J. R. Primack, Contraction of Dark Matter Galactic Halos Due to Baryonic Infall, Astrophys. J. **301**, 27 (1986).
- [42] O. Y. Gnedin, A. V. Kravtsov, A. A. Klypin, and D. Nagai, Response of dark matter halos to condensation of baryons: Cosmological simulations and improved adiabatic contraction model, Astrophys. J. **616**, 16 (2004), arXiv:astro-ph/0406247.
- [43] S. Mashchenko, J. Wadsley, and H. M. P. Couchman, Stellar Feedback in Dwarf Galaxy Formation, Science **319**, 174 (2008), arXiv:0711.4803 [astro-ph].

- [44] F. Governato *et al.*, At the heart of the matter: the origin of bulgeless dwarf galaxies and Dark Matter cores, *Nature* **463**, 203 (2010), arXiv:0911.2237 [astro-ph.CO].
- [45] R. H. Dicke, The measurement of thermal radiation at microwave frequencies, *Review of Scientific Instruments* **17**, 268 (1946), <https://doi.org/10.1063/1.1770483>.
- [46] Y.-H. Chang *et al.*, Taiwan Axion Search Experiment with Haloscope, (2022).
- [47] B. Brubaker, L. Zhong, S. Lamoreaux, K. Lehnert, and K. van Bibber, Haystac axion search analysis procedure, *Physical Review D* **96**, 10.1103/physrevd.96.123008 (2017).
- [48] A. Savitzky and M. J. E. Golay, Smoothing and differentiation of data by simplified least squares procedures, *Anal. Chem.* **36**, 1627 (1964).